Applied Catalysis B: Environmental 237 (2018) 1059–1065

Contents lists available at ScienceDirect

Applied Catalysis B: Environmental

journal homepage: www.elsevier.com/locate/apcatb

Role of hydrogen absorption in supported Pd nanocatalysts during CO-PROX: Insights from *operando* X-ray absorption spectroscopy

Claudia Zlotea[a,*], Yassine Oumellal[a], Karine Provost[a], Franck Morfin[b], Laurent Piccolo[b,*]

[a] Université Paris Est, Institut de Chimie et des Matériaux Paris-Est (UMR 7182), CNRS, UPEC, 2-8 rue Henri Dunant, F-94320, Thiais, France
[b] Univ Lyon, Université Claude Bernard - Lyon 1, CNRS, IRCELYON - UMR 5256, 2 Avenue Albert Einstein, F-69626, VILLEURBANNE CEDEX, France

ARTICLE INFO

Keywords:
Pd catalyst
CO oxidation
Preferential oxidation of CO in H_2 excess
Operando X-ray absorption spectroscopy

ABSTRACT

The nature of the active phase (metallic *vs.* oxidic, metal phase *vs.* concentrated hydride/ dilute solid solution with hydrogen) in heterogeneous catalysis by supported metals is still a matter of high debate. Here, we have monitored for the first time oxide-supported Pd nanocatalysts (average particle size 4.5 nm) during both CO oxidation (in H_2-free atmosphere) and preferential oxidation of CO in H_2 excess (PROX) by *operando* X-ray absorption spectroscopy. Under our conditions, the CO conversion in the absence of H_2 is around 30% at 150 °C and reaches 100% at 200 °C, whereas in the presence of H_2 the conversion reaches a maximum of 15% (at 250 °C), in agreement with our previous works using a conventional flow-fixed bed reactor. The active phase for CO oxidation below 200 °C is metallic Pd, whereas it is a solid solution of Pd with hydrogen during PROX below 300 °C. This work provides a direct evidence of the presence of subsurface/bulk hydrogen as a probable cause of the low PROX performance of supported Pd catalysts.

1. Introduction

In the context of pollution-free power sources, proton exchange membrane fuel cells (PEMFCs) require the use of high purity hydrogen. Currently, hydrogen is mainly produced from fossil sources through catalytic steam reforming, with CO traces still present in the gas stream even after the separation processes (1–100 ppm). CO is well known to be a poison for Pt-based anodes, and thus to reduce the number of active sites available for H_2 adsorption/dissociation and oxidation reactions. Thus, PEMFCs require the use of ultrapure hydrogen gas supply, which can be achieved by previous separation with Pd-based membrane, catalytic methanation or catalytic preferential oxidation of CO (PROX) in the presence of hydrogen. The latter reaction is mainly catalyzed by platinum-group metals [1–3], but transition metal oxides are also promising [4–6].

In this context, the identification of the oxidation state and the local structure of the catalyst during CO oxidation conditions (in the presence or absence of hydrogen) is of key importance for understanding the involved catalytic mechanisms. Conventional laboratory techniques are difficult to employ in order to highlight these features mainly because of high dispersion and small metal content of the catalyst on the support. Due to its atomic selectivity and high sensitivity, X-ray Absorption Spectroscopy (XAS) is a powerful tool for characterizing both the oxidation state and the local order of supported catalysts under reactive environment. Several XAS investigations have already revealed the local structure of a variety of catalysts for CO oxidation [5–8] and PROX [4]. However, *operando* studies during PROX are scarce [4,6,9] and they mainly concern mixed oxides monitored at the transition metal K-edge during steady-state reaction [4,6]. Sasmaz et al. have investigated the local structure of Pd catalysts supported on CeO_2 and MnO_x-CeO_2 during CO oxidation [9]. The authors have shown by EXAFS analysis that PdO is formed on both supports after oxidation in air at 250 °C. Sintering and redispersion of Pd is noticed on CeO_2 during H_2 treatment and subsequent oxidation by exposure to air, whereas PdO is partially reduced by CO and forms a mixture of Pd^{n+} and Pd^0 species during CO oxidation.

In this work, we report, for the first time, a comparative *operando* XAS study of CO oxidation and PROX over a Pd-based catalyst. The catalytic performances for both reactions of this Pd/SiO_2-Al_2O_3 catalyst in a conventional flow fixed bed reactor have been previously reported [2]. A full conversion of CO was reached above 200 °C, whereas only 20% of CO was converted in PROX at 250 °C. Here, we use *operando* XAS to investigate the atmosphere-dependent Pd phase in order to determine the corresponding active phases at the origin of these activity differences.

* Corresponding authors.
E-mail addresses: claudia.zlotea@icmpe.cnrs.fr (C. Zlotea), laurent.piccolo@ircelyon.univ-lyon1.fr (L. Piccolo).

https://doi.org/10.1016/j.apcatb.2018.06.059
Received 17 April 2018; Received in revised form 18 June 2018; Accepted 22 June 2018
Available online 23 June 2018
0926-3373/

2. Experimental details

2.1. Synthesis and characterization of Pd/ASA catalyst

The oxide-supported Pd nanocatalyst has been prepared by incipient wetness impregnation of amorphous silica-alumina (ASA, 40 wt% SiO_2, 500 m^2/g) with Pd(II) acetylacetonate dissolved in toluene, followed by decomposition of the Pt precursor under hydrogen at up to 500 °C. The metal loading was 0.89 wt% and the average size of Pd nanoparticles was 4.5 ± 1.2 nm. More details on the synthetic procedure and the physicochemical properties of Pd/ASA catalyst are given elsewhere [2,10,11].

2.2. Operando X-ray absorption spectroscopy

The local structure of the supported Pd nanoparticles was investigated by X-ray absorption spectroscopy (XAS) in transmission mode on the ROCK beam line at the SOLEIL synchrotron. X-ray absorption spectra were recorded at the Pd K edge at fixed temperatures. The powder samples were placed inside a Lytle-type cell, which was connected to a gas distribution system that allows a careful control of the gas flow at atmospheric pressure [12]. The samples were loaded under air and *in situ* pre-treated under hydrogen flow at room temperature to remove the oxide at the surface of the nanoparticles, as previously demonstrated for different supported Pd nanoparticles [13].

Four steps of *operando* XAS experiments were performed, as depicted in Fig. 1.

The four steps consisted of the following protocol:

Step 1) Treatment under H_2 flow (15 ml min^{-1}) during heating from room temperature to 250 °C followed by cooling from 250 to 60 °C. XAS spectra were recorded only during cooling at 250, 200, 150, 100 and 60 °C.

Step 2) Treatment under He flow (40 ml· min^{-1}) during heating from 60 to 300 °C. XAS spectra were recorded at 60, 100, 150, 200, 250 and 300 °C. The reduction of the catalyst was followed by a treatment under He to avoid the formation of palladium hydride.

Step 3) CO oxidation reaction during cooling from 300 to 100 °C. XAS spectra were recorded at 300, 250, 200, 150 and 100 °C.A gas mixture of 1.56% CO + 1.56% O_2 in He (15 ml· min^{-1}) was used for this *operando* experiment.

Step 4) PROX reaction during heating from 100 to 300 °C. XAS spectra were recorded at 100, 150, 200, 250 and 300 °C.A gas mixture of 1.56% CO + 1.56% O_2 + 37.5% H_2 in He (15 ml· min^{-1}) was used for this *operando* experiment.

This procedure does not induce nanoparticle coalescence, as previously proven [10].

The XAS measurements were supplemented by continuous mass spectrometry (MS) monitoring to make sure that a catalytic regime was reached, determine the reaction kinetics, and thereby properly correlate structural and catalytic data.

The XAS data treatment and EXAFS refinements were performed with the MAX program package (E_0 = 24,350 eV for Pd K edge, Fourier transform range 4 - 14 $Å^{-1}$) [14,15]. XANES spectra were normalized and calibrated in energy. EXAFS fitting was performed on first-sphere filtered spectra for Pd in metal/hydride/solid solution states and on fourth-sphere filtered spectra for the oxidized Pd catalyst. Theoretical phases and amplitudes were computed with FEFF8 on the basis of either metallic Pd phase (*fcc* structure, $Fm\bar{3}m$, a = 3.89 Å) [16] or PdO phase (tetragonal structure, $P4_2/mmc$, a = 3.03 Å and c = 5.33 Å) [9]. The refined parameters are the coordination number (N), the Debye-Waller factor (σ^2) and the first-neighbour distance ($R_{Pd\text{-}X(Pd\ or\ O)}$) of each shell. The energy shift ΔE_0 was refined first for the bulk Pd reference and then fixed for further refinements. The goodness of fit was evaluated using the quality factor (QF).

For oxidized nanoparticles, the number of different Pd-Pd distances was evaluated as proposed by Moscovici et al. [17] by following the QF evolution when the number of shells increases.

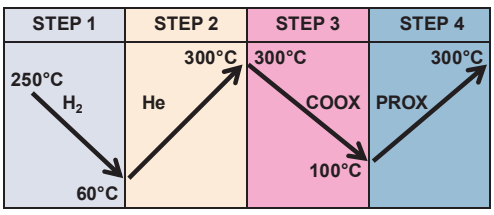

Fig. 1. The four steps of the *operando* XAS experiment.

3. Results

Experimental EXAFS spectra recorded during the four steps and the corresponding FT modules are shown in Figs. 2–5. The results of EXAFS refinements are listed in Table 1.

For comparison, we have also recorded the XAS spectra of bulk Pd under air. The refined parameters obtained for bulk Pd (N, σ^2 and $R_{Pd\text{-}Pd}$) are in very good agreement with previous results [18,19].

The XANES regions of XAS spectra for the Pd/ASA catalyst under different environments (hydrogen, helium, CO oxidation and PROX) at 100 and 300 °C are plotted in Figure SI-1. All spectra are comparable at 100 °C, irrespective of gas environment, whereas at 300 °C the XANES spectrum is significantly different under CO oxidation than under PROX and inert gas, suggesting important changes in the Pd electronic state and atomic environment. Moreover, we observed an energy-shift of around 5 eV towards higher energies compatible with partial oxidation of Pd [20,21] and an important change in the first oscillations, indicating modifications of the average Pd atomic environment.

3.1. Step 1: Cooling from 250 to 60 °C under H_2 flow

Under H_2 flow at atmospheric pressure, the EXAFS and FT signals change with temperature (Fig. 2).

In k-space, we observed a slight phase shift between the spectra recorded at 250, 200 and 150 °C and the ones recorded at lower temperatures, compatible with a change in the distances of the Pd-Pd first sphere.

In R-space, the maximum of the FT amplitude increases with decreasing temperature (from 250 to 150 °C) due to the decrease in thermal disorder (see the Debye-Waller factor in Table 1). Then, at 100 °C it decreases slightly and shifts to higher $R_{Pd\text{-}Pd}$ distances as compared to 150 °C, and enhances again at 60 °C without any detectable shift of the $R_{Pd\text{-}Pd}$ distance. The decrease in FT amplitude from 150 to 100 °C can be reasonably explained by an increase in static disorder introduced by hydrogen insertion into the metal lattice, as also noticed for bulk Pd hydride that experiences a larger σ^2 (0.0080 $Å^2$) as compared to the pure Pd metal under air (0.0066 $Å^2$) at room temperature (Table 1). At 60 °C, the FT amplitude increases again due to decreased thermal disorder relative to the FT peak amplitude at 100 °C.

EXAFS refinements for Pd nanoparticles under H_2 are based on the *fcc* structure of the bulk metal (Table 1). The coordination number varies in the range 8.8–9.4 (± 0.8) and is smaller than 12, typical for bulk Pd. This can be accounted by the small size of Pd/ASA nanoparticles (~4.5 nm) relative to bulk, as already proven for other metal nanoparticles [16,19,22]. Our previous TEM measurements suggested nanoparticles with a roughly spherical shape [2]. Thus, the present values of the coordination number in the first shell are in agreement with earlier results obtained for spherical nanoparticles with similar sizes [23].

Surprisingly, during cooling from 250 to 150 °C, the $R_{Pd\text{-}Pd}$ distances undergo a slight expansion from 2.738(3) to 2.753(3) Å (Table 1). Then, the $R_{Pd\text{-}Pd}$ distance increases from 2.753(3) Å at 150 °C to 2.796(2) Å at 100 °C and 2.807(2) Å at 60 °C. This latter trend can be understood in terms of Pd hydride formation during cooling under H_2

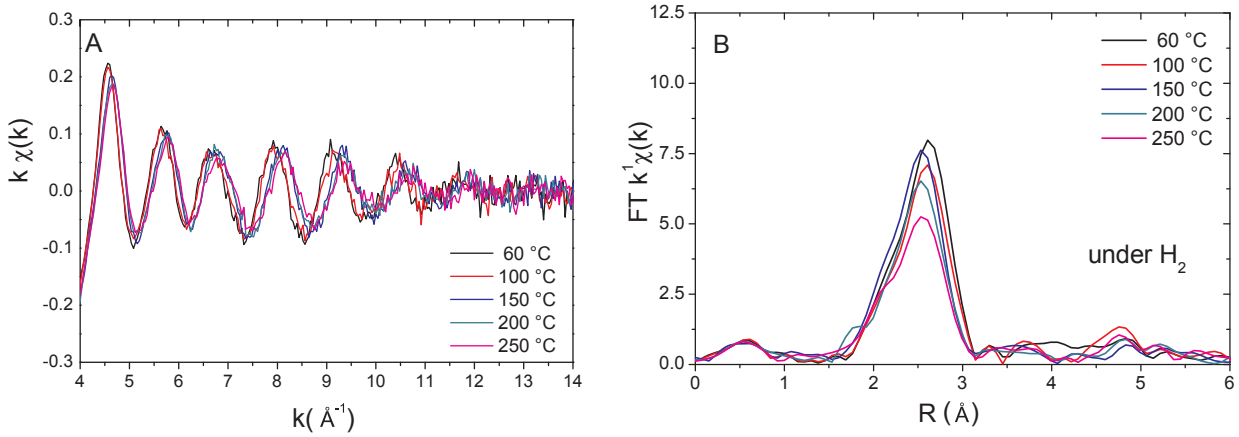

Fig. 2. Experimental EXAFS spectra at Pd K edge (A) and corresponding modules of the Fourier transforms (B) for Pd/ASA under H_2 flow during cooling from 250 to 60 °C.

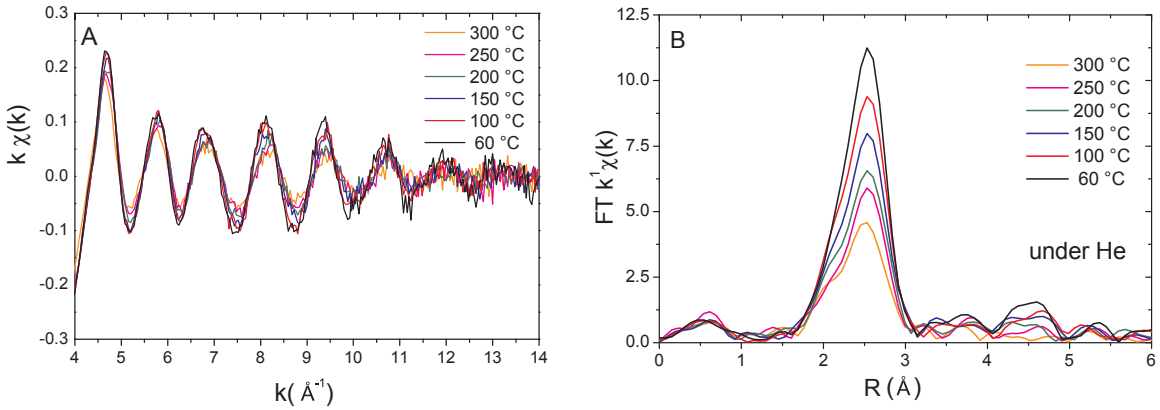

Fig. 3. Experimental EXAFS spectra at Pd K edge (A) and corresponding modules of the Fourier transforms (B) for Pd/ASA under He flow during heating from 60 to 300 °C.

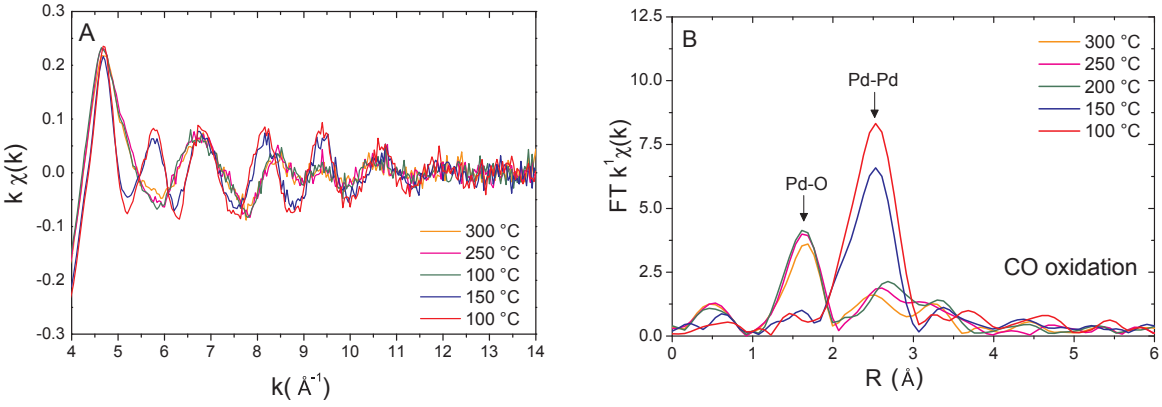

Fig. 4. Experimental EXAFS spectra at Pd K edge (A) and corresponding modules of the Fourier transforms (B) for Pd/ASA during cooling from 300 to 100 °C under CO oxidation conditions.

flow. Indeed, from the thermodynamics of the reaction with hydrogen gas, a bulk Pd hydride phase ($PdH_{0.7}$) can be formed under certain H_2 pressure and temperature conditions. We have used a flow of pure H_2 at 1 bar and an equilibrium pressure of 1 bar H_2 occurs at 127 °C, as calculated from the enthalpy and entropy values for bulk Pd: $\Delta H = -36.7$ kJ/mol H_2 and $\Delta S = -92$ J/K/molH_2 [24]. Thus, below this temperature and under 1 bar H_2, the Pd hydride phase is likely to form, whereas above this threshold, only solid solutions and metallic Pd are expected. A solid solution of Pd with hydrogen (PdH_x with $x < 0.1$) is formed by absorption of a small hydrogen quantity within the metal phase with hydrogen atoms randomly occupying the interstitial sites of the *fcc* structure. On the contrary, the hydride phase (PdH_x with $x \sim 0.6$) absorbs a large amount of hydrogen atoms and their occupancy of the interstitial sites is ordered. Thus, Pd forms a hydride at 60 and 100 °C, whereas only solid solutions with hydrogen and/or metal phases are present above 150 °C.

3.2. Step 2: Heating from 60 to 250 °C under He flow

At the end of step 1, Pd is in the form of a hydride phase under H_2

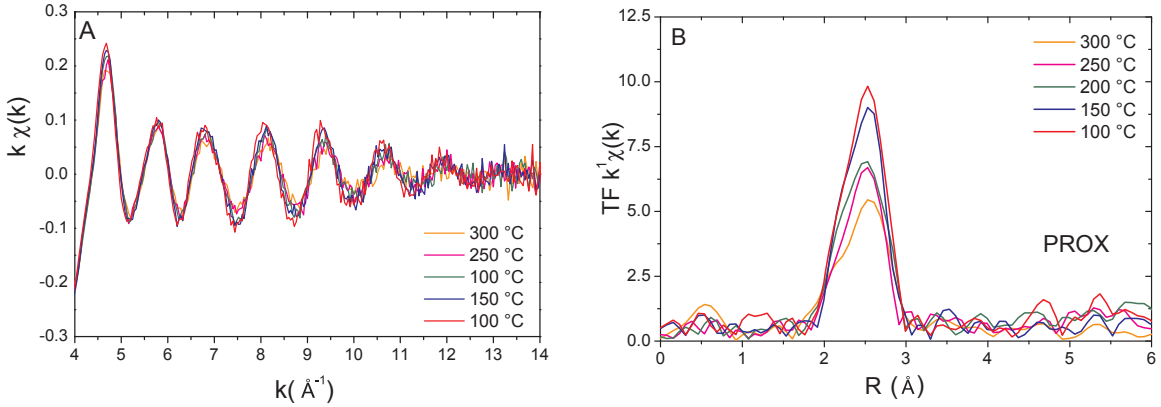

Fig. 5. Experimental EXAFS spectra at Pd K edge (A) and corresponding modules of the Fourier transforms (B) for Pd/ASA during heating from 100 to 300 °C under PROX conditions.

Table 1
Results of EXAFS refinements for Pd/ASA nanoparticles under different gaseous environments: coordination number (*N*), Debye-Waller factor (σ^2), nearest neighbour distance ($R_{Pd\text{-}X}$) for each shell and quality of fit (QF). Results for bulk Pd under air and under hydrogen atmosphere [18,19] are also given for comparison.

Sample	Gas	T (°C)	Pd K edge						
			Shell	Pd *fcc*			PdO tetragonal			
				N (Pd)	σ^2 (Å^2)	$R_{Pd\text{-}Pd}$ (Å)	*N* (*X*)	σ^2 (Å^2)	$R_{Pd\text{-}X}$ (Å)	QF
Pd bulk	air	25	1: Pd-Pd	11.7(6)	0.0066(2)	2.744(1)	–	–	–	4.09
	H_2 [18,19]	25		12	0.0080	2.840	–	–	–	–
Pd/ASA	H_2	250	1: Pd-Pd	9.3(8)	0.0145(7)	2.738(3)	–	–	–	0.24
		200		8.8(8)	0.0122(4)	2.747(4)	–	–	–	0.74
		150		9.4(8)	0.0116(3)	2.753(3)	–	–	–	0.56
		100		9.0(8)	0.0116(6)	2.796(2)	–	–	–	0.33
		60		9.4(7)	0.0110(5)	2.807(2)	–	–	–	0.42
	He	60	1: Pd-Pd	8.8(5)	0.0089(2)	2.751(2)	–	–	–	0.04
		100		9.3(6)	0.0103(4)	2.744(2)	–	–	–	0.03
		150		9.3(7)	0.0113(4)	2.736(2)	–	–	–	0.02
		200		8.5(7)	0.0120(7)	2.727(3)	–	–	–	0.03
		250		8.8(5)	0.0134(4)	2.728(5)	–	–	–	0.03
		300		8.8(7)	0.0161(7)	2.735(6)	–	–	–	0.04
	CO oxidation	300	1: Pd-O	–	–	–	4.4(6)	0.009(2)	1.99(1)	1.74
			2: Pd-Pd	1.4(5)	0.009(2)	2.70(1)	–	–	–	
			3: Pd-Pd	–	–	–	1.8(7)	0.009(2)	3.41(2)	
		250	1: Pd-O	–	–	–	4.7(6)	0.009(1)	1.99(1)	1.89
			2: Pd-Pd	1.2(4)	0.009(1)	2.72(1)	–	–	–	
			3: Pd-Pd	–	–	–	2.1(6)	0.009(1)	3.39(2)	
		200	1: Pd-O	–	–	–	4.9(8)	0.009(2)	1.99(1)	3.62
			2: Pd-Pd	1.2(6)	0.009(2)	2.72(2)	–	–	–	
			3: Pd-Pd	–	–	–	2.3(6)	0.009(2)	3.39(2)	
		150	1: Pd-Pd	9.0(5)	0.0124(5)	2.734(4)	–	–	–	0.06
		100	1: Pd-Pd	8.7(5)	0.0107(3)	2.742(3)	–	–	–	0.05
	PROX	100	1: Pd-Pd	9.2(3)	0.0105(2)	2.757(2)	–	–	–	0.02
		150		9.2(4)	0.0108(2)	2.745(2)	–	–	–	0.03
		200		9.5(4)	0.0121(3)	2.740(2)	–	–	–	0.02
		250		9.4(6)	0.0133(5)	2.738(4)	–	–	–	0.03
		300		10.0(5)	0.0147(2)	2.730(2)	–	–	–	0.01

flow at 60 °C. The switch from H_2 to He does not significantly changes the shapes of EXAFS and FT signals, as compared to the ones under H_2 at similar temperature. However, it is well known that Pd hydride is not stable and desorbs hydrogen under inert gas or vacuum at room temperature [24]. Thus, all refinements under He flow have been done using the archetypical *fcc* Pd metal structure (Table 1).

During this step, there is no change in the edge position as compared to spectra recorded under H_2 atmosphere (Figure SI-1), and no phase shift is observed in k-space. The most visible change in k-space is the decrease of the amplitude of oscillations simultaneously to the decrease of the FT amplitude in the R-space with increasing the temperature (Fig. 3). This finding can be explained by an increase in the Debye-Waller factor due to an enhancement of the dynamic thermal disorder with temperature (see Table 1). At 60 °C and 100 °C, the $R_{Pd\text{-}Pd}$ distances are significantly lower than those obtained under H_2 atmosphere, indicating that all the hydrogen has been released. Similarity to the previous case, the $R_{Pd\text{-}Pd}$ distances undergo a slight contraction from 2.751(2) to 2.735(6) Å with increasing the temperature. We can conclude that Pd is metallic during this step, irrespective of the temperature.

3.3. Step 3: Cooling under CO oxidation flow conditions

At the end of step 2, Pd is metallic and the introduction of the reactive gas mixture induces significant changes of both XANES (Figure SI-1) and EXAFS (Fig. 4) signals. For temperatures lower or equal to 150 °C, the edge position is similar for H_2, He or CO oxidation conditions, while for higher temperatures, a clear shift towards high energies

is observed under CO oxidation as compared to H_2 and He (Figure SI-1). Concerning EXAFS, for lower temperatures (100–150 °C), the spectra are similar to those observed under H_2 and He conditions, with a main peak in the R-space around 2–3 Å compatible with Pd-Pd first neighbours in the *fcc* structure. For higher temperatures (200–300 °C), the signal is completely different: we observe completely different phases in the k-space, and the FT presents a main peak 1–2 Å compatible with oxygen neighbours around Pd absorbing atoms [9].

The EXAFS refinements for spectra recorded between 300 and 200 °C were performed taking into account the possibility of a partial oxidation of nanoparticles. The tetragonal PdO crystal structure possesses the first Pd-O shell with 4 neighbouring O atoms at 2.01 Å, and two Pd-Pd shells (4 Pd neighbours at 3.03 Å and 8 Pd neighbours at 3.42 Å [9]), while in the Pd *fcc* structure, each Pd atom is surrounded by 12 Pd neighbours at 2.74 Å. These different distances lead to a large overlapping of the Pd-O and the several Pd-Pd signals. In particular, the large peak between 2 and 4 Å may be related to three different Pd-Pd signals (Fig. 4). Therefore, for oxidized nanoparticles, EXAFS refinements were performed on 0–4 Å filtered spectra using a model with a first Pd-O shell and 1 to 3 different Pd-Pd shells. To limit correlations effects, we used a unique σ^2 for all shells. The best refinement was obtained for a three-shell model (1 Pd-O from PdO + 1 Pd-Pd from *fcc* metal + 1 Pd-Pd from PdO), (Table 1) that suggests an oxide structure at nanoscale slightly different from the crystalline bulk PdO.

In the presence of three strongly overlapping signals (one Pd-O shell and two Pd-Pd shell with different phases), it is difficult to obtain precise amplitude parameters, since such a situation implies not only correlations between amplitude parameters, but also between amplitude and phase parameters [25]. This may explain the unexpected low σ^2 and large $N_{Pd\text{-}O}$ values obtained for these refinements ($\sigma^2 \sim 0.008$-0.009 Å^2 and $N_{Pd\text{-}O} \sim 4.4$–4.9). The obtained value of σ^2 is smaller and the error bars larger than the ones under inert gas at similar temperatures. The comparison between the experimental and fitted filtered EXAFS and FT signals for the best refinement in the case of th Pd catalyst under CO oxidation conditions at 300 °C is shown in Figure SI-2.

The significant amount of O neighbours (4.4–4.9) at a distance compatible with the Pd-O distance in crystalline PdO confirms the strong oxidation of the nanoparticles. Interestingly, the two $R_{Pd\text{-}Pd}$ distances obtained in the refinement are 2.70–2.72 Å and 3.38–3.41 Å. The first Pd-Pd distance is close to the one for the Pd nanocatalyst under inert gas (2.735(6) Å at 300 °C), while the second one is in good agreement with the 2nd Pd-Pd shell in crystalline PdO, within the error bars. The clear presence of Pd neighbours around 2.71 Å indicates that metallic Pd species are still present at these temperatures, but in a very limited amount ($N \sim 1.2$–1.4). Therefore, we can conclude that between 200 and 300 °C, the Pd nanocatalyst is partially oxidized. Similar trend was noticed for Pd/CeO_2 and Pd/MnO_x-CeO_2 catalysts during CO oxidation by Sasmaz et al. [9] These authors used a similar combined structural model (PdO and Pd) and found a value of $N \sim 2$ for the Pd-Pd shell originating from the *fcc* metal structure.

Below 200 °C, the EXAFS refinements have been successfully performed within the structural model of *fcc* Pd metal (Table 1). The FT profiles at 100 and 150 °C are typical for metallic Pd with $N = 8.7$–9.0 for the first shell, in good agreement with the values obtained for the Pd catalyst under He and H_2 flows. The $R_{Pd\text{-}Pd}$ values at these temperatures are very close to the ones under He flow at the same temperatures (Table 1). This hints to metallic Pd under CO oxidation below 200 °C.

In summary, during CO oxidation at temperatures above 200 °C, the Pd catalyst is oxidized. However, oxidation is not complete since metallic Pd species are still present, although in a very limited amount. Below this threshold in temperature, the Pd catalyst is completely reduced to metallic Pd. This feature can be explained by the reducing effect of CO, the coverage of which increases as temperature decreases due to both residence time and reaction effects. Indeed, the mass spectrometry data of Figure SI-3 show that the extinction temperature of CO oxidation occurs below 200 °C. Under our CO oxidation conditions, which are over-stoichiometric in O_2, the CO/O_2 ratio abruptly increases below this temperature. The observed reduction of Pd ions in the presence of CO is also consistent with a previous EXAFS study of Pd nanoparticles supported on La-stabilized alumina, showing the reduction of PdO at 140 °C during exposure to CO [26].

3.4. Step 4: Heating from 100 to 300 °C under PROX flow conditions

At the end of step 3, the Pd catalyst is completely reduced to the metal state. Under PROX conditions, the XANES (Figure SI-1) and EXAFS spectra (Fig. 5) spectra are similar to those observed under H_2 and He environments.

In k-space we can only notice a decrease of the oscillation amplitude accompanied by a similar trend of TF amplitude with increasing the temperature. As explained before, this feature can be reasonably accounted for by the increase in thermal disorder with temperature.

From the thermodynamics of hydride formation in bulk Pd, an equilibrium pressure of 375 mbar H_2 (the partial pressure of H_2 in the PROX reaction conditions) is only expected below 94 °C, meaning that the hydride phase is stable below this temperature. Thus, only solid solutions with hydrogen (PdH_x with $x < 0.1$) and/or metallic Pd phases are expected to form in our conditions (375 mbar H_2 and above 100 °C).

4. Discussion

The thermal variation of $R_{Pd\text{-}Pd}$ for the Pd/ASA catalyst in different gaseous environments is plotted in Fig. 6.

Under He flow, the Pd catalyst is metallic with a surprising slight contraction of $R_{Pd\text{-}Pd}$ distances as temperature increases from 60 up to 200 °C. For higher temperatures, this distance starts to smoothly increase, in agreement with an expected thermal expansion.

Under H_2 flow at atmospheric pressure, the Pd hydride phase is formed below 100 °C, as expected from thermodynamic considerations for bulk metal. This is in good agreement with the larger values of $R_{Pd\text{-}Pd}$ distance at 60 and 100 °C relative to higher temperatures (Fig. 6). This expansion is due to the hydrogen absorption and the ordered occupation of the interstitial sites of the *fcc* structure. Above 100 °C, the hydride phase is not stable and the $R_{Pd\text{-}Pd}$ distances are smaller than the values obtained at lower temperatures under H_2 but larger than the ones under He flow. This can be accounted for the formation of solid solutions of Pd with hydrogen and slight expansion of the first-neighbour distance under H_2 flow. Moreover, as also noticed under He flow in the temperature range 60–200 °C, the thermal trend of $R_{Pd\text{-}Pd}$ under H_2 flow shows an unexpected slight contraction above 150 °C.

Under CO oxidation conditions, Pd is in metallic state only at 100

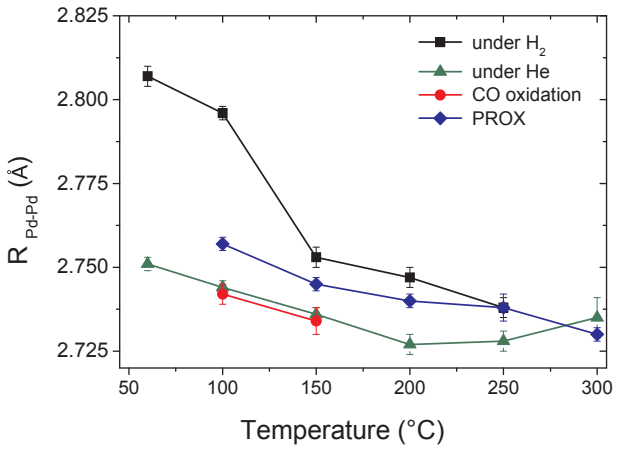

Fig. 6. Thermal evolution of the first-neighbour distance $R_{Pd\text{-}Pd}$ for the Pd/ASA catalyst under different gaseous environments (H_2 and He) and reactive conditions (CO oxidation and PROX).

and 150 °C and the values of $R_{Pd\text{-}Pd}$ are very similar to the ones obtained under inert gas at these temperatures. Above 150 °C, Pd is oxidized but metallic Pd species are still present although in a very limited amount.

Under PROX conditions, the $R_{Pd\text{-}Pd}$ distances are larger than the values under inert gas in the temperature range 100–250 °C. Since no hydride phase is expected under these conditions, we can conclude that Pd forms a solid solution with hydrogen. At 300 °C, the $R_{Pd\text{-}Pd}$ value is close to the one under inert gas (within the error bar), suggesting that Pd is metallic and the initial small amount of absorbed hydrogen is desorbed. Similarly to the previous cases, the $R_{Pd\text{-}Pd}$ distances under PROX conditions show an anomalous decrease with increasing the temperature (Fig. 6).

This "negative thermal expansion", which occurs for all gaseous environments used during this experiment, is believed to originate from a combination of nanosize and metal-oxide interaction effects. Moreover, this seems to be a more general trend for metals, since a similar behaviour was already reported for γ-alumina-supported Pt nanoparticles [27,28]. Very recently, a theoretical study highlighted that anomalous properties, such as negative thermal expansion and large structural disorder (as determined by EXAFS), arise from synergistic effects of limited dimensionality of these nanoparticles, intraparticles heterogeneity and oxide support [29]. These authors suggested that a combination of thermal vibrations and low-frequency disorder can explain this behaviour, as supported by finite temperature DFT/MD simulations. However, our very recent *in situ* XAS results demonstrated that such a thermal behaviour does not occur for carbon-supported Rh nanoparticles despite their small size (around 1.4 nm) [30]. Thus, we hypothesize here that the negative thermal expansion observed for Pd nanoparticles might be due to a complex combination of both nanosize and strong interaction with the oxide support.

From the MS data (Figure SI-3), we have determined the CO_2 formation rate under CO oxidation and PROX reaction conditions. The MS results are in good agreement with our previous study obtained with a conventional flow-fixed bed reactor [2]. Fig. 7 correlates these MS results with the Pd catalyst state and local structure, as determined by *operando* XAS.

Under CO oxidation conditions, Pd is metallic only at 100 and 150 °C and shows a significant catalytic activity above 100 °C (ca. 30% CO conversion at 150 °C), in agreement with earlier results [31]. Above 150 °C, CO conversion is 100% and a mixture of Pd^{2+} and Pd° species is present. However, under this reaction regime, a gradient of reactant concentrations is present along the catalyst bed, with no CO at the outlet of the bed. Under such an oxidizing atmosphere and our working temperatures (above 150 °C), Pd is subjected to oxidation (explaining the XAS detection of Pd oxide). Thus, a gradient of Pd oxidation states throughout the catalyst bed might exist, making it difficult to conclude on the nature of the active phase in this 100% CO conversion regime. In contrast, from the data at 150 °C, we can reliably conclude that the catalytically active phase is metallic Pd, although the oxidation state of Pd under CO oxidation conditions is still under debate [9,32–34].

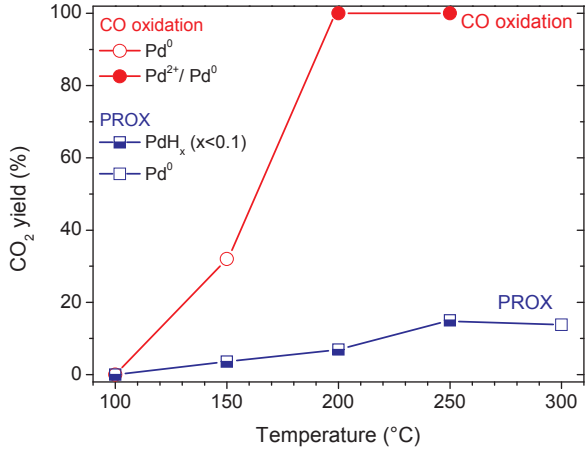

Fig. 7. CO_2 yield during CO oxidation and PROX over Pd/ASA, as measured by MS during XAS experiments. Empty, half-filled and full symbols stand for metallic Pd, solid solution PdH_x ($x < 0.1$) and mixed Pd^{2+}/Pd° species, respectively, as determined from EXAFS refinements.

The Pd catalyst is active under PROX conditions above 100 °C, leading to the formation of CO_2, H_2O and, above 200 °C, CH_4 (see Figure SI-3), with a maximum CO_2 yield of ca. 15% at 250 °C (Fig. 7), in agreement with the low CO_2 selectivity of Pd catalysts measured in our laboratory tests [2]. This hints to a relatively modest activity of the Pd solid solution with hydrogen towards the CO conversion in H_2 excess. This conclusion is also consistent with our previous study on the PROX performances of alumina and ASA-supported Pd(-Ir) nanocatalysts (alumina and ASA gave similar results) [2]. Moreover, from the correlation between catalytic and hydrogen sorption measurements, we had recently suggested that the low activity of Pd in PROX (comparatively to other Pt-group metals, Pd-Ir nanoalloys, and Pd performance in H_2-free CO oxidation) was due to the formation of a Pd hydride (concentrated hydrogen phase) and/or a solid solution with hydrogen (dilute hydrogen phase) [11]. As previously reported by Pozdnyakova et al. using *in situ* XPS, the poor activity of a Pd/CeO_2 catalyst in CO-PROX (also recently substantiated in our comparison of the platinum-group metals supported on ceria [3]) could be explained by the poor selectivity of the Pd hydride towards CO oxidation with respect to H_2 oxidation [35]. However, these *in situ* XPS experiments have been performed under 0.45 mbar of H_2 at two temperatures (358 and 523 K). Under these conditions the Pd hydride phase is not thermodynamically stable and spontaneously desorbs hydrogen, forming a solid solution with hydrogen [24]. Here, we have directly demonstrated, by using a local structural probe under *operando* conditions, that the active Pd phase contains subsurface/bulk hydrogen in a solid solution phase. Hence, the small hydrogen absorption is likely to be responsible for the low CO-PROX performance of the Pd catalyst as compared to standard CO oxidation. It can be inferred that interstitial hydrogen atoms can readily diffuse back towards the Pd surface, making it very active for undesirable hydrogen oxidation. Under favourable thermodynamic and kinetic conditions, the subsurface is replenished with hydrogen incoming from the gas phase.

The above examples for a wide range of supports (alumina, silica-alumina and ceria) in terms of acidity and reducibility suggest that, although the performances can be quantitatively different depending on the support, the poorness of Pd in CO-PROX is a general result ascribable to hydrogen absorption in Pd. Thus, in the light of these results combined with our previous findings, one possible route to improve the efficiency of Pd-based catalysts for the PROX reaction is the tuning of the chemical composition of metal nanoparticles (for example, by nanoalloying, as we proposed recently [11]) in order to hamper the hydrogen absorption into the bulk/subsurface. This strategy may also apply to other hydrogen-involving catalytic reactions, such as selective hydrogenations of hydrocarbons [36,37].

5. Conclusions

We have performed an *operando* XAS investigation of oxide-supported Pd nanocatalysts (average size 4.5 nm) in both H_2-free CO oxidation and CO-PROX. These measurements were complemented by continuous mass spectroscopy to properly correlate structural and catalytic data. The CO conversion (in H_2-free atmosphere) is around 30% at 150 °C and reaches 100% at 200 °C. On the contrary, the CO conversion under PROX conditions is much less and reaches a maximum of 15% at 250 °C. The EXAFS refinements prove that, under our conditions, the active phase for CO oxidation is metallic Pd at 150 °C, whereas PdH_x ($x < 0.1$) solid solution (with $x = 0$ only at 300 °C) is active in PROX above 100 °C. Thus, we clearly demonstrated that the low PROX activity of the Pd catalyst strongly correlates with the

presence of subsurface/bulk hydrogen. This opens the way for designing non-absorbing hydrogen Pd-based catalysts through chemical modification in order to improve their performance for catalytic reactions under hydrogen-rich atmospheres.

Acknowledgments

Fabrice Couturas and Stéphanie Belin are warmly acknowledged for help during the XAS experiments at SOLEIL. The work at the ROCK beam line at the SOLEIL synchrotron, was supported by a public grant overseen by the French National Research Agency (ANR) as part of the "Investissements d'Avenir" program (reference: ANR-10-EQPX-45).

Appendix A. Supplementary data

Supplementary material related to this article can be found, in the online version, at doi:https://doi.org/10.1016/j.apcatb.2018.06.059.

References

[1] K. Liu, A. Wang, T. Zhang, Recent advances in preferential oxidation of CO reaction over platinum group metal catalysts, ACS Catal. 2 (2012) 1165–1178, http://dx.doi.org/10.1021/cs200418w.
[2] F. Morfin, S. Nassreddine, J.L. Rousset, L. Piccolo, Nanoalloying effect in the preferential oxidation of CO over Ir-Pd catalysts, ACS Catal. 2 (2012) 2161–2168, http://dx.doi.org/10.1021/cs3003325.
[3] T.-S. Nguyen, F. Morfin, M. Aouine, F. Bosselet, J.-L. Rousset, L. Piccolo, Trends in the CO oxidation and PROX performances of the platinum-group metals supported on ceria, Catal. Today 253 (2015) 106–114, http://dx.doi.org/10.1016/j.cattod.2014.12.038.
[4] R. Zhang, J.T. Miller, C.D. Baertsch, Identifying the active redox oxygen sites in a mixed Cu and Ce oxide catalyst by in situ X-ray absorption spectroscopy and anaerobic reactions with CO in concentrated H2, J. Catal. 294 (2012) 69–78, http://dx.doi.org/10.1016/j.jcat.2012.07.005.
[5] T. Cwele, N. Mahadevaiah, S. Singh, H.B. Friedrich, A.K. Yadav, S.N. Jha, D. Bhattacharyya, N.K. Sahoo, CO oxidation activity enhancement of Ce0.95Cu0.05O2-[small delta] induced by Pd co-substitution, Catal. Sci. Technol. 6 (2016) 8104–8116, http://dx.doi.org/10.1039/C6CY00981F.
[6] L. Lukashuk, K. Föttinger, E. Kolar, C. Rameshan, D. Teschner, M. Hävecker, A. Knop-Gericke, N. Yigit, H. Li, E. McDermott, M. Stöger-Pollach, G. Rupprechter, Operando XAS and NAP-XPS studies of preferential CO oxidation on Co3O4 and CeO2-Co3O4 catalysts, J. Catal. 344 (2016) 1–15, http://dx.doi.org/10.1016/j.jcat.2016.09.002.
[7] J. Highfield, T. Liu, Y.S. Loo, B. Grushko, A. Borgna, Skeletal Ru/Cu catalysts prepared from crystalline and quasicrystalline ternary alloy precursors: characterization by X-ray absorption spectroscopy and CO oxidation, Phys Chem Chem Phys. 11 (2009) 1196–1208, http://dx.doi.org/10.1039/B811775F.
[8] A.V. Malyutin, A.I. Mikhailichenko, Y.V. Zubavichus, V.Y. Murzin, A.G. Koshkin, I.V. Sokolov, Effect of metal-support interaction in the M/Ce0.72Zr0.18Pr0.1O2 (M = Ru, Pd, and Pt) catalysts and their activity in CO and CH4 oxidation, Kinet. Catal. 56 (2015) 89–105, http://dx.doi.org/10.1134/S0023158415010097.
[9] E. Sasmaz, C. Wang, M.J. Lance, J. Lauterbach, In situ spectroscopic investigation of a Pd local structure over Pd/CeO2 and Pd/MnOx-CeO2 during CO oxidation, J. Mater. Chem. A. 5 (2017) 12998–13008, http://dx.doi.org/10.1039/C7TA00696A.
[10] L. Piccolo, S. Nassreddine, M. Aouine, C. Ulhaq, C. Geantet, Supported Ir–Pd nanoalloys: Size–composition correlation and consequences on tetralin hydroconversion properties, J. Catal. 292 (2012) 173–180, http://dx.doi.org/10.1016/j.jcat.2012.05.010.
[11] C. Zlotea, F. Morfin, T.S. Nguyen, N.T. Nguyen, J. Nelayah, C. Ricolleau, M. Latroche, L. Piccolo, Nanoalloying bulk-immiscible iridium and palladium inhibits hydride formation and promotes catalytic performances, Nanoscale 6 (2014) 9955–9959, http://dx.doi.org/10.1039/c4nr02836h.
[12] C. La Fontaine, L. Barthe, A. Rochet, V. Briois, X-ray absorption spectroscopy and heterogeneous catalysis: performances at the SOLEIL's SAMBA beamline, Operando IV 4th Int. Congr. Operando Spectrosc. 205 (2013) 148–158, http://dx.doi.org/10.1016/j.cattod.2012.09.032.
[13] C. Zlotea, Y. Oumellal, K. Provost, C. Matei Ghimbeu, Experimental challenges in studying hydrogen absorption in ultra-small metal nanoparticles, Front. Energy Res. 4 (2016) 24, http://dx.doi.org/10.3389/fenrg.2016.00024.
[14] A. Michalowicz, J. Moscovici, D. Muller-Bouvet, K. Provost, for XAFS, J. Phys, MAX: multiplatform applications, Conf. Ser. 190 (2009) 012034.
[15] A. Michalowicz, J. Moscovici, D. Muller-Bouvet, K. Provost, MAX (multiplatform applications for XAFS) New features, J. Phys. Conf. Ser. 430 (2013) 012016.
[16] A. Malouche, G. Blanita, D. Lupu, J. Bourgon, J. Nelayah, C. Zlotea, Hydrogen absorption in 1 nm Pd clusters confined in MIL-101(Cr), J. Mater. Chem. A. (2017), http://dx.doi.org/10.1039/C7TA07159K.
[17] J. Moscovici, A. Rougier, S. Laruelle, A. Michalowicz, Apparent mismatch between extended x-ray absorption fine structure and diffraction structures of crystalline metastable WO3 phases, J. Chem. Phys. 125 (2006) 124505, http://dx.doi.org/10.1063/1.2357148.
[18] C. Zlotea, F. Cuevas, V. Paul-Boncour, E. Leroy, P. Dibandjo, R. Gadiou, C. Vix-Guterl, M. Latroche, Size-dependent hydrogen sorption in ultrasmall Pd clusters embedded in a mesoporous carbon template, J. Am. Chem. Soc. 132 (2010) 7720–7729, http://dx.doi.org/10.1021/ja101795g.
[19] Y. Oumellal, K. Provost, C.M. Ghimbeu, A.M. de Yuso, C. Zlotea, Composition and size dependence of hydrogen interaction with carbon supported bulk-immiscible Pd–Rh nanoalloys, Nanotechnology 27 (2016) 465401.
[20] D. Grandjean, R.E. Benfield, C. Nayral, A. Maisonnat, B. Chaudret, EXAFS and XANES study of a pure and Pd doped novel Sn/SnOx nanomaterial, J. Phys. Chem. B. 108 (2004) 8876–8887, http://dx.doi.org/10.1021/jp0370627.
[21] J. Nilsson, P.-A. Carlsson, H. Grönbeck, M. Skoglundh, First principles calculations of palladium nanoparticle XANES spectra, Top. Catal. 60 (2017) 283–288, http://dx.doi.org/10.1007/s11244-016-0612-0.
[22] A.I. Frenkel, C.W. Hills, R.G. Nuzzo, A View from the inside: complexity in the atomic scale ordering of supported metal nanoparticles, J. Phys. Chem. B. 105 (2001) 12689–12703, http://dx.doi.org/10.1021/jp012769j.
[23] A. Jentys, Estimation of mean size and shape of small metal particles by EXAFS, Phys Chem Chem Phys. 1 (1999) 4059–4063, http://dx.doi.org/10.1039/A904654B.
[24] W.A. Oates, Thermodynamic properties of the Pd-H system, J. Common. Met. 88 (1982) 411–424.
[25] K. Provost, E.C. Beret, D. Muller, E.S. Marcos, A. Michalowicz, Impact of the number of fitted Debye-Waller factors on EXAFS fitting, J. Phys. Conf. Ser. 430 (2013) 012015.
[26] J.R. Gaudet, A. de la Riva, E.J. Peterson, T. Bolin, A.K. Datye, Improved Low-temperature CO oxidation performance of Pd supported on La-stabilized alumina, ACS Catal. 3 (2013) 846–855, http://dx.doi.org/10.1021/cs400024u.
[27] J.H. Kang, L.D. Menard, R.G. Nuzzo, A.I. Frenkel, Unusual Non-bulk properties in nanoscale materials: thermal metal−metal bond contraction of γ-alumina-supported Pt catalysts, J. Am. Chem. Soc. 128 (2006) 12068–12069, http://dx.doi.org/10.1021/ja064207p.
[28] S.I. Sanchez, L.D. Menard, A. Bram, J.H. Kang, M.W. Small, R.G. Nuzzo, A.I. Frenkel, The emergence of nonbulk properties in supported metal clusters: negative thermal expansion and atomic disorder in Pt nanoclusters supported on γ-Al2O3, J. Am. Chem. Soc. 131 (2009) 7040–7054, http://dx.doi.org/10.1021/ja809182v.
[29] F.D. Vila, J.J. Rehr, R.G. Nuzzo, A.I. Frenkel, Anomalous structural disorder in supported Pt nanoparticles, J. Phys. Chem. Lett. 8 (2017) 3284–3288, http://dx.doi.org/10.1021/acs.jpclett.7b01446.
[30] C. Zlotea, L. Blondeau, A. Malouche, J. Bourgon, K. Provost, F. Morfin, L. Piccolo, Investigation of the local structure of nanosized rhodium hydride, J. Colloid Interface Sci. 524 (2018) 427–433, http://dx.doi.org/10.1016/j.jcis.2018.04.047.
[31] K. Zorn, S. Giorgio, E. Halwax, C.R. Henry, H. Grönbeck, G. Rupprechter, CO oxidation on technological pd−al2o3 catalysts: oxidation State and activity, J. Phys. Chem. C. 115 (2011) 1103–1111, http://dx.doi.org/10.1021/jp106235x.
[32] M.A. van Spronsen, J.W.M. Frenken, I.M.N. Groot, Surface science under reaction conditions: CO oxidation on Pt and Pd model catalysts, Chem. Soc. Rev. 46 (2017) 4347–4374, http://dx.doi.org/10.1039/C7CS00045F.
[33] G. Sitja, C.R. Henry, Molecular beam study of the oxidation of carbon monoxide on a regular array of palladium clusters on alumina, J. Phys. Chem. C. 121 (2017) 10706–10712, http://dx.doi.org/10.1021/acs.jpcc.6b10706.
[34] V. Bratan, C. Munteanu, C. Hornoiu, A. Vasile, F. Papa, R. State, S. Preda, D. Culita, N.I. Ionescu, CO oxidation over Pd supported catalysts —In situ study of the electric and catalytic properties, Appl. Catal. B Environ. 207 (2017) 166–173, http://dx.doi.org/10.1016/j.apcatb.2017.02.017.
[35] O. Pozdnyakova, D. Teschner, A. Wootsch, J. Kröhnert, B. Steinhauer, H. Sauer, L. Toth, F.C. Jentoft, A. Knop-Gericke, Z. Paál, R. Schlögl, Preferential CO oxidation in hydrogen (PROX) on ceria-supported catalysts, part II: oxidation states and surface species on Pd/CeO2 under reaction conditions, suggested reaction mechanism, J. Catal. 237 (2006) 17–28, http://dx.doi.org/10.1016/j.jcat.2005.10.015.
[36] A. Valcarcel, F. Morfin, L. Piccolo, Alkene hydrogenation on metal surfaces: why and when are Pd overlayers more efficient catalysts than bulk Pd? J. Catal. 263 (2009) 315–320, http://dx.doi.org/10.1016/j.jcat.2009.02.023.
[37] H.A. Aleksandrov, S.M. Kozlov, S. Schauermann, G.N. Vayssilov, K.M. Neyman, How absorbed hydrogen affects the catalytic activity of transition metals, Angew. Chem. Int. Ed. 53 (2014) 13371–13375, http://dx.doi.org/10.1002/anie.201405738.